Materials & Design 215 (2022) 110489

Contents lists available at ScienceDirect

Materials & Design

journal homepage: www.elsevier.com/locate/matdes

Design guidelines for suppressing distortion and buckling in metallic thin-wall structures built by powder-bed fusion additive manufacturing

G. Vastola [a,*], W.J. Sin [b], C.-N. Sun [b], N. Sridhar [a]

[a] A*STAR Institute of High Performance Computing, 1 Fusionopolis Way, #16-16 Connexis, Singapore 138632, Singapore
[b] A*STAR Singapore Institute of Manufacturing Technology, 2 Fusionopolis Way, Singapore 138634, Singapore

HIGHLIGHTS

- Smooth corners reduce distortion in metallic thin-wall tubular components made by powder-bed fusion additive manufacturing.
- Self-buckling is the primary mode of distortion and part width has a stronger impact on distortion compared to part height.
- Experiments confirm tubular cross-sections exhibit significantly lower distortion than those with a square-like cross-section.

GRAPHICAL ABSTRACT

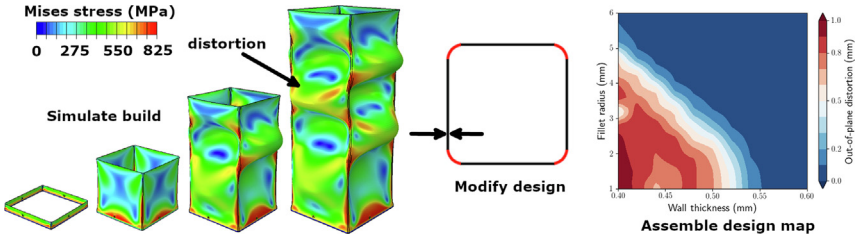

ARTICLE INFO

Article history:
Received 22 November 2021
Revised 8 February 2022
Accepted 23 February 2022
Available online 5 March 2022

Keywords:
Design for additive manufacturing
Distortion
Modeling and simulation
Design map

ABSTRACT

Controlling distortion in laser powder-bed fusion additive manufacturing is of critical importance especially for thin-wall structures, which typically experience significant deformation and buckling during the build process. We examine this issue from the perspective of design by systematically performing numerical simulations of the additive process of tubular components as a function of part design, including fillet radius, wall thickness, tube width and height. It is found that round corners, as opposed to sharp corners, suppress distortion even at small wall thickness (400 μm), while part width has a greater impact on distortion than part height. The buckling behavior of such structures is numerically investigated and analysis results show that for designs most prone to distortion, a critical height exists below which the component is distortion-free. The modeling was experimentally validated by manufacturing thin-wall components of IN718 alloy using the EOS M290 printer. The findings provide practical guidelines to manufacture metallic thin-wall tubular components with minimal to no distortion using powder-bed fusion additive manufacturing.

1. Introduction

Continuous insertion of laser powder-bed fusion (L-PBF) additive manufacturing (AM) into industrial production is driving sustained growth in this sector, recording a 7.5% YoY growth in 2020 [1]. Compared to traditional manufacturing, L-PBF is economically viable for complicated parts, such as jet engine fuel nozzles [2], aerospace icing sensors [2], hydraulic manifolds [3], and radiofrequency antennas for space applications [4] since AM allows the part to be built in one piece, instead of individually manufacturing each component and then assembling them. Further, the case for AM is compelling for lightweight parts, where AM enables lattice structures to be easily incorporated [5]. The aerospace sector is particularly poised to reap the benefits of this technology.

Powder-bed fusion additive manufacturing is the process whereby thin layers of powder (thickness 20–90 μm) are spread by a recoater blade in a chamber of controlled atmosphere [6].

* Corresponding author.
E-mail address: vastolag@ihpc.a-star.edu.sg (G. Vastola).

https://doi.org/10.1016/j.matdes.2022.110489

After slicing the CAD file of the part into layers, a laser or an electron beam selectively scans and melts the powder to reproduce one slice of the CAD file. After melting and solidification of one layer is complete, the build platform is lowered by a layer thickness, the recoater spreads a new layer of powder, and the process continues until the part is complete.

Because melting is extremely localized, manufacturing is accompanied by significant thermal gradients (of the order of 10^4 K/cm [7]). Therefore, substantial thermal stresses are generated in regions surrounding the melt pool, usually exceeding the yield strength of the material. As a result, the residual stresses remain in the part after build, accompanied by part distortion [8]. Often, the stresses are sufficient to induce cracking before the build is complete [9] resulting in significant waste of powder and machine time.

Numerical predictions for part distortion is an active field of research where the residual stresses and distortion are predicted with computer modeling. By simulating the additive process before the actual part build, issues are identified early, and compensation measures such as modifications of the CAD file and alteration of part orientation in the build chamber can be implemented. Hodge *et al.* [10] developed a sequential thermo-mechanical calculation based on proprietary software, showing the details of the residual stress field changing from compressive to tensile while moving from the bottom to the top of the part. The model was further applied to wedge and L-shapes [11], and the simulations showed good agreement with neutron-diffraction measurements. Prabhakar et al. [12] developed an effective-layer thermo-mechanical model where a "hot" layer is deposited at once, thermal gradients are computed, and then a mechanical calculation follows. Sequential thermo-mechanical calculations have also been developed for powder-bed fusion of single and multiple tracks [13 14] (including for relatively large sequences of scan vectors [15]), and for the wire-feed and Directed Energy Deposition (DED) processes [16 17]. Of particular relevance here, Huang *et al.* developed a layer heating method which, coupled with a mechanical solver, was able to predict residual stresses in tubular samples with good accuracy [18]. Collectively, they highlight numerical simulations as a valid tool to investigate distortion in PBF-AM components and provide the numerical foundation for Design for Additive Manufacturing (DfAM) [19]. DfAM workflow investigates how the PBF-AM process alters the part shape, introducing deviations in the original drawing, and explores alternative designs that minimizes the impact of the manufacturing process. In this context, we note that thin-wall structures are notoriously difficult shapes to build, due to their significant distortion. This issue has been investigated from the point of view of modifying the process parameters, in an attempt to find parameters that mitigate distortion. Yang *et al.* [20] investigated the role of process parameters in the microstructure and distortion of L-shaped samples, suggesting alternative scan strategies to reduce residual stress. Calignano *et al.* proposed a set of process parameters for the case of AlSi10Mg alloy [21] showing an improved match between the original part drawing and the final part. While process parameters do affect distortion, their modification appears insufficient especially when the manufacturability limits of the printer are reached. For example, Ahmed *et al.* reported very large distortion at a wall thickness of 0.5 mm in PBFAM of AlSi10Mg [22], where distortion reduces by increasing wall thickness.

Because thin-wall structures are a key component to functional products such as heat exchangers [23] and antennas [24], distortion minimization is of paramount importance for the application of such components in industrial applications. To the best of our knowledge, a systematic study is unreported for distortion in tubular components from the standpoint of design. So, in this paper, we numerically and experimentally investigate the role of part design in the distortion of thin-wall tubular components. We summarize our results in terms of two "design maps", one for distortion and the other for buckling, which can be directly used by the practitioner as a guide to reduce distortion in such components.

2. Methods

Our numerical analysis is based on the inherent-strain, or eigenstrain, method [25]. In this method, an initially-defined strain value (the inherent strain) is assigned to each mesh element [26 27] and represents the amount of plastic strain that the material experienced due to processing. In other words, given that the total strain ε is the sum of elastic (ε_e), plastic (ε_p), thermal (ε_{th}), and transformational strain (ε_{tr})

$$\varepsilon = \varepsilon_e + \varepsilon_p + \varepsilon_{th} + \varepsilon_{tr} \tag{1}$$

the final component distortion and residual stresses are the result of the inelastic portion of the total strain. Therefore, the inherent strain ε^* is defined as:

$$\varepsilon - \varepsilon_e = \varepsilon_p + \varepsilon_{th} + \varepsilon_{tr} = \varepsilon^* \tag{2}$$

In the seminal work by Doo Jang *et al.* [28], there was good agreement between predicted and measured distortion for welding of a ship hull block. Later, Kim *et al.* [29] introduced a thermal model to correlate the inherent strain to thermal gradients and showed good predictions for the distortion and residual stress for butt welding of thin plates. Assuming a fully-constrained elastic-perfectly plastic constitutive relationship and ignoring phase transformational strains, the inherent strain arising from one complete heating-cooling thermal cycle is $\varepsilon^* = -Y/E$, where Y is the yield strength and E is the Young's modulus of the material [29]. During heating, the compressive plastic strain can exceed the elastic limit; then, as the material cools down, thermal shrinking partially relieves the plastic strain, ultimately leaving an amount $-Y/E$. [29]. We recognize that ε^* may need to be estimated more precisely to accurately capture the global distortion (for example as in the Ti6Al4V material system [30]), especially in terms of the transformational strain; however, such an accurate estimation is beyond the scope of this work.

After assigning each mesh element with an initial strain ε^*, the stress $\boldsymbol{\sigma}$ and strain $\boldsymbol{\varepsilon}$ fields are derived from the displacement field $\boldsymbol{u}$ through the classical constitutive law:

$$\boldsymbol{\sigma} = \boldsymbol{C} : \varepsilon^{el} = C : (\varepsilon - \varepsilon^* - \varepsilon^p), \tag{3}$$

where $\boldsymbol{\varepsilon}^{el}$ is the elastic strain, $\boldsymbol{\varepsilon}$ is the total strain tensor for large deformations $\varepsilon_{ij} = \frac{1}{2}\left(\frac{\partial u_i}{\partial x_j} + \frac{\partial u_j}{\partial x_i}\right) + \frac{1}{2}\frac{\partial u_k}{\partial u_i}\frac{\partial u_k}{\partial u_j}$ in which $\boldsymbol{u} = (u_x, u_y, u_z)$ is the displacement field and $\boldsymbol{x}$ is the position vector. Here, $\boldsymbol{C}$ is the tensor of elastic constants the components of which depend on E and ν, and $\boldsymbol{\varepsilon}^p$ is the plastic strain tensor. Mechanical equilibrium was recomputed after the addition of each mesh layer to mimic the additive process.

The thin wall tubular component shown in Fig. 1 was chosen as starting point for the analysis, where the shape was characterized by two parameters, namely the wall thickness and the fillet radius. The material chosen was the IN718 alloy. The inherent strain method was implemented in the ABAQUS software (Dassault Systèmes, Providence, RI, USA) using python scripting. The inherent strain ε^* was applied as a thermal strain using a fictitious temperature increment of 1 and a thermal expansion coefficient equal to ε^*. IN718 was modeled as a plastically anisotropic material with the yield strength along the build direction lower than that of the in-plane, to account for the effect of processing on mechanical properties, as declared by the material and machine supplier [31]. In particular, the following values were used: $E = 160\ GPa$, $Y_{vertical} = 780\ MPa$, $Y_{in-plane} = 634\ MPa$, $\nu = 0.23$, corresponding to a Hill's criterion for anisotropic plasticity parameter

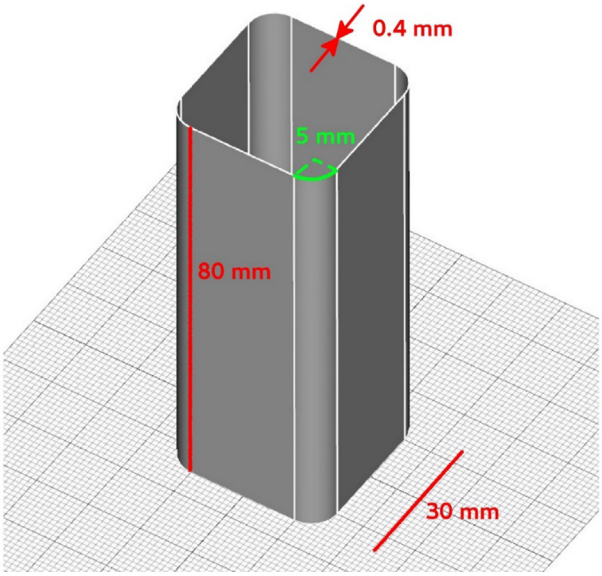

Fig. 1. Drawing of the thin-wall structure, for the case of 5 mm fillet radius (in green) and 400 μm wall thickness. (For interpretation of the references to color in this figure legend, the reader is referred to the web version of this article.)

$R_{33} = 0.812820$. Therefore, $\varepsilon^* = -0.004875$ in our calculations. Although anisotropic mechanical properties are included in the material model, the same value of inherent strain was applied to both the in-plane and the build direction.

We implemented a python script in Abaqus to carry out the analysis in a sequence of steps, whereby in each step, one mesh layer was added. The mesh element type was S4R (quadrilateral, large-strain shell element) and the element size was 500 μm. Such value was chosen after performing mesh sensitivity analysis which showed that, for the component of interest, distortion was captured with reasonable accuracy while the computational time remained low. The script created the thin wall geometry, the mesh, assigned elements to layers, assigned material properties (including the inherent strain), and the step definition. In total, the mesh consisted of 38232 elements and 160 mesh layers. To account for inaccuracies and imprecision of the actual manufacturing process, a small imperfection was added at the bottom of the mesh. Numerically, this imperfection was necessary to break the perfect symmetry of the mesh, which allowed distortion to emerge. We checked that the results were not dependent on the magnitude and location of the imperfection. Run time, including geometry meshing and slicing, was only 15 min using 16 Intel® Xeon® E5-2650 cores. A contributing factor to the short run time was the implementation of an efficient algorithm for meshing and slicing, whereby identification of the elements belonging to the same layer (slicing) was performed before runtime within a single loop over elements, therefore saving the time of identifying new layer elements at runtime.

The three-dimensional distortion shape and linear vertical distortion profile using a wall thickness of 0.4 mm, fillet radius of 1 mm, are shown in Fig. 2 (a) and (b), respectively, where the distortion of panel (a) is magnified by a factor of 10 to improve visibility. Significant distortion, up to about 0.8 mm, is predicted along the wall height.

Starting from the layer-by-layer simulation of an individual tubular component, we further developed a python script to encapsulate this calculation into a systematic workflow, to investigate how distortion responded to changes in part design. The design parameters considered were the wall thickness and fillet radius. We illustrate this workflow in Fig. 3 and discuss the results in the next Section.

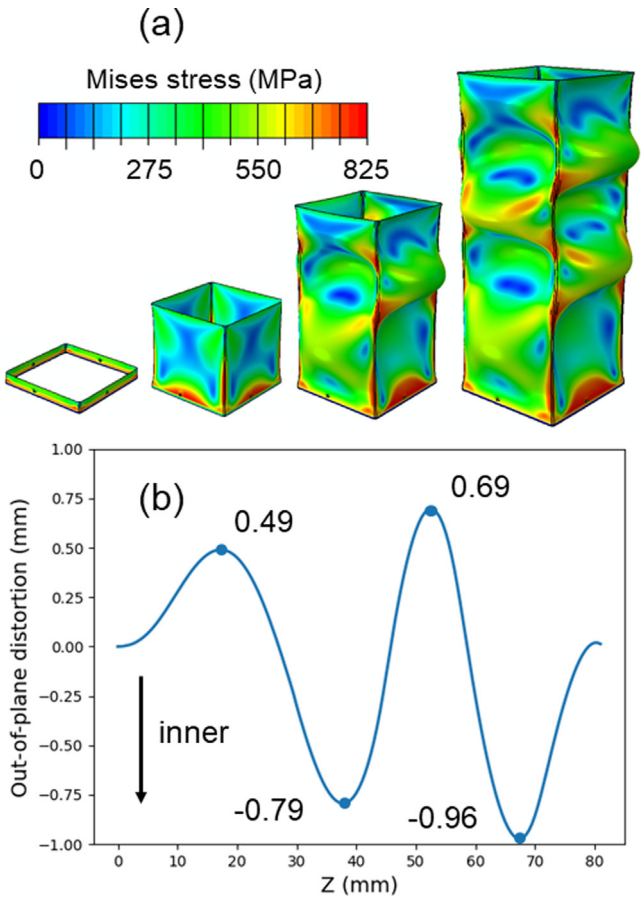

Fig. 2. (a) Three-dimensional computed distortion in square thin-wall structure with wall thickness of 0.4 mm and fillet radius of 1 mm, where distortion was magnified by 10 to aid visualization. Color shows Von Mises stress in MPa. (b) vertical displacement profile along mid-wall, with extremals values marked for clarity. The inner side of component is reported with an arrow.

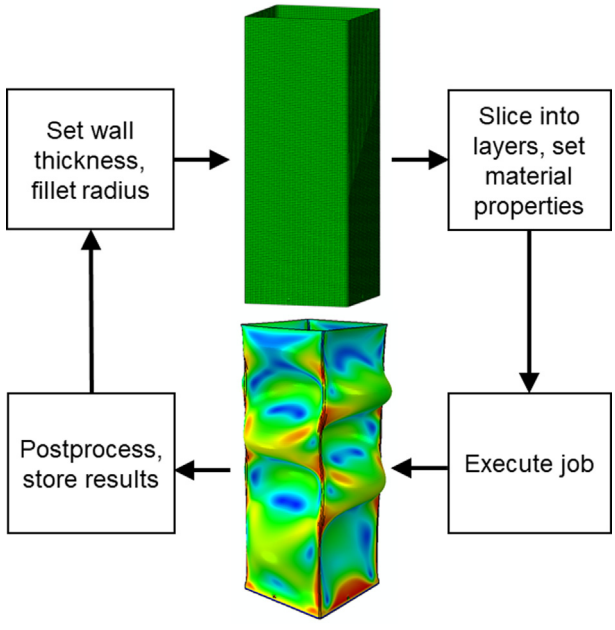

Fig. 3. Workflow for systematic calculations of part distortion as a function of design parameters (wall thickness, fillet radius).

To further investigate and understand the distortion mechanism, buckling analysis was performed. It is worth recalling that the eigenvalues of a numerical buckling analysis are load factors that, when multiplied by the applied load, determine buckling of the pre-stressed structure. In the present scenario, the loads are the residual stresses generated by the manufacturing process, and we are interested in eigenvalues equal to one since this would signal that the applied load is sufficient to buckle the thin wall, implying that the component would self-buckle. Noting the height at which the first eigenvalue reaches one gives the critical height beyond which the thin wall buckles, and hence severely distorts. The numerical procedure was implemented as follows. For each combination of wall thickness and fillet radius, mesh and layer slicing was performed as in the case of an individual calculation, described previously. However, we repeat this process N times, where N is the number of mesh layers of the final part, and we add a buckling analysis step for the last added layer, where the load is set to the inherent strain added to that last layer. This way, eigenvalues and eigenshapes extraction predict the onset of buckling as the wall height increases. Fig. 4 shows the schematic of this analysis, which we implemented through additional Abaqus python scripting.

Experimental validations were performed by manufacturing thin-wall samples on a selective laser melting (SLM) machine model M290 (EOS GmbH, Krailling, Germany) equipped with a 400 W Yb-fiber laser. The powder material was EOS Inconel 718 with particle sizes ranging from 20 μm to 55 μm [31]. Process parameters were optimized for a layer thickness of 40 μm with 80 °C build platform preheating. The fillet radius was varied from 1 to 15 mm and the wall thickness was varied from 0.4 to 1 mm. Samples were fabricated with one edge being oriented towards the recoating direction (i.e. thin-wall at a 45-degree angle to the recoating direction) to reduce the impact force exerted by the interaction between the built part and the hard recoater blade. Representative thin-wall designs are shown in Fig. 5.

After removal from the baseplate by electrical discharge machining (EDM) wire cutting, the samples were analyzed with a structured-light 3D scanning device (Breuckmann smartSCAN-HE 4.0, AICON 3D Systems GmbH) for image reconstruction. The scanned images were examined by 3D inspection software (PolyWorks Inspector, InnovMetric Software) to quantitatively extract the distortion values.

The summary of the design parameters explored, their range, and experimental verification work are reported in Table 1.

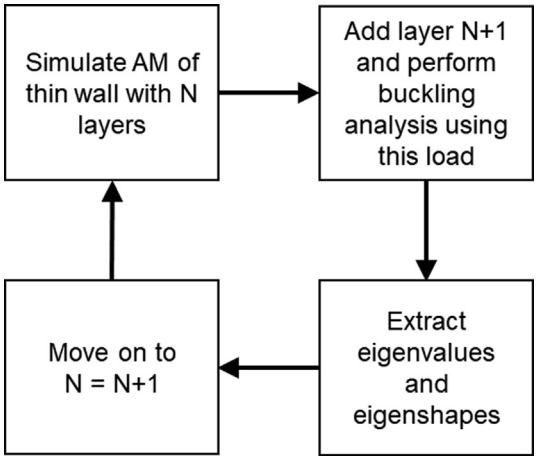

Fig. 4. Workflow for numerical calculation of critical load for self-buckling during additive manufacturing using the inherent strain method.

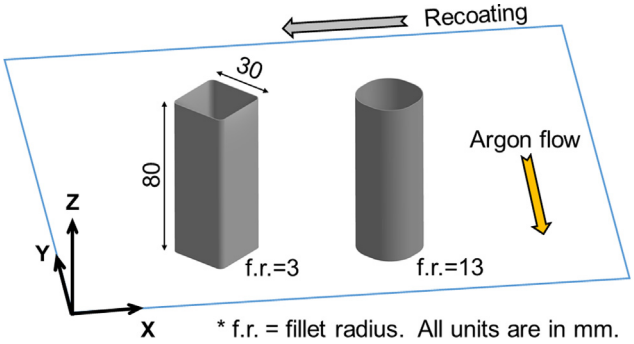

Fig. 5. Geometry of the representative thin-wall designs with wall thickness of 0.4 mm and fillet radius of 1 mm. The schematic is based on EOS M290 machine setup.

Table 1
Summary of numerical and experimental combinations of wall thickness, fillet radius, part width, and height explored in this work.

	Simulations (mm)	Experiments (mm)
Wall thickness	0.4–0.6	0.4–0.6
Fillet radius	1–6	1–6
Part width	15,30,45	30
Part height	40,80,120	80

3. Results and discussion

For each combination of wall thickness and fillet radius, the Abaqus python script generated the geometry and the mesh, performed the calculation with the inherent strain and post-processed the results. Output files were post-processed to extract the maximum distortion (i.e., the maximum out-of-plane displacement from the reference shape) as a function of the two design parameters. Color-coding the values resulted in the design map of Fig. 6. To achieve a high resolution, the wall thickness was explored from 0.4 mm to 0.6 with a step size of 0.02 mm, while the fillet radius was explored from 1 mm to 6 mm with a step size of 0.1 mm. Therefore, each design map comprising 561 calculations. The large number of calculations required was the reason

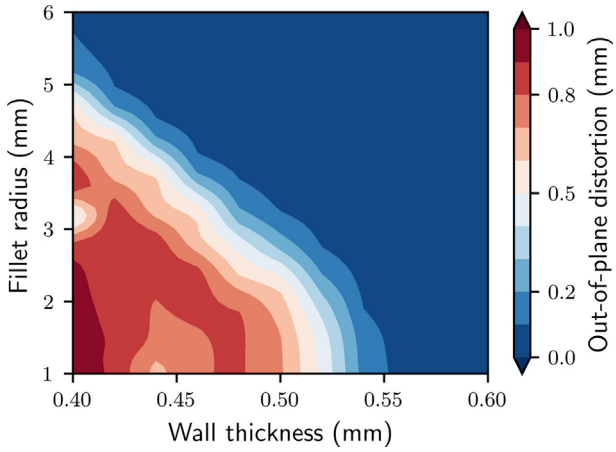

Fig. 6. Design map plotting the maximum out-of-plane distortion of a thin-wall structure as a function of wall thickness and fillet radius. Blue color represents low to no distortion, while red color represents significant distortion, which is quantified in the color bar. The actual distorted part at wall thickness 0.4 mm and fillet radius 1 mm is shown in Fig. 2(a). (For interpretation of the references to color in this figure legend, the reader is referred to the web version of this article.)

why a mesh size of 0.5 mm, and not a smaller one, was used, which allowed each calculation to run within a reasonable amount of time (15 min). The effect of increasing the wall thickness decreases distortion, as intuition suggests. More interestingly, an increase in the fillet radius also resulted in a decreased distortion. We note that the increase in the fillet radius progressively transforms the design from a square tube into a cylindrical tube. Therefore, the design map suggests that cylindrical shapes are less prone to buckling compared to square tubes for a given circumferential cross-section. Rounded corners, as opposed to sharp corners, reduce the likelihood of distortion in the component. Since sharply rounded corners, as well as thin walls, are a general template for many component shapes, we believe this finding is applicable more broadly, beyond simple tubular components.

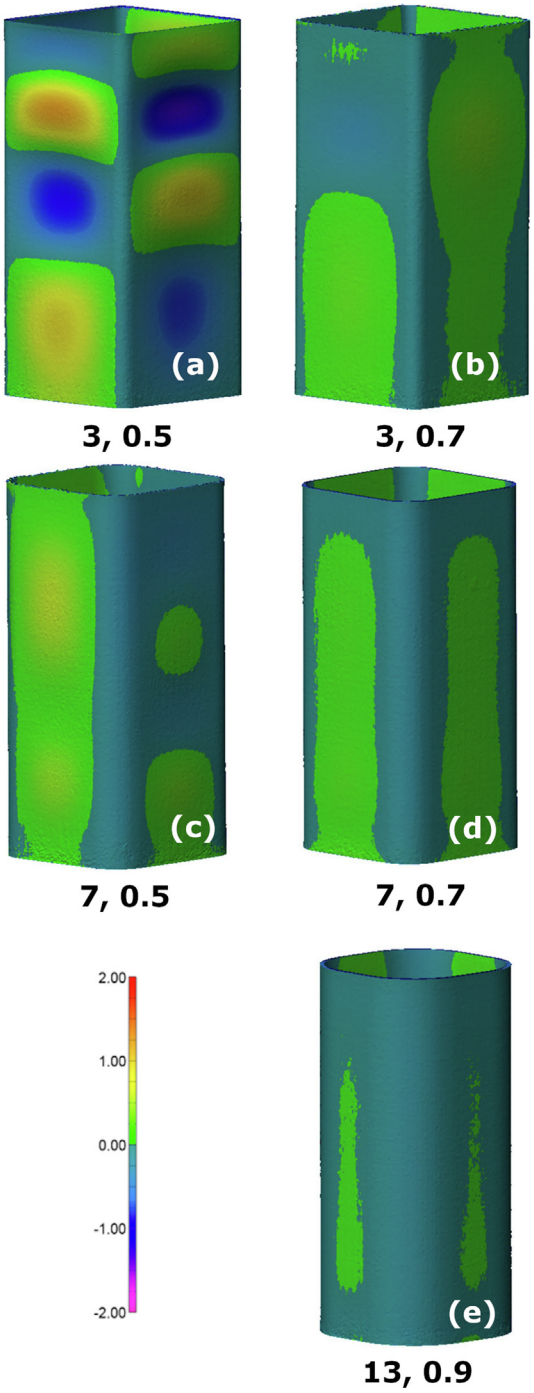

Fig. 7. Three-dimensional laser scans of thin wall components for different choices of fillet radius and wall thickness, confirming the reduced distortion for tubular components as compared to square-cross section designs. The labels are in the format of fillet radius in millimetres followed by wall thickness in millimetres.

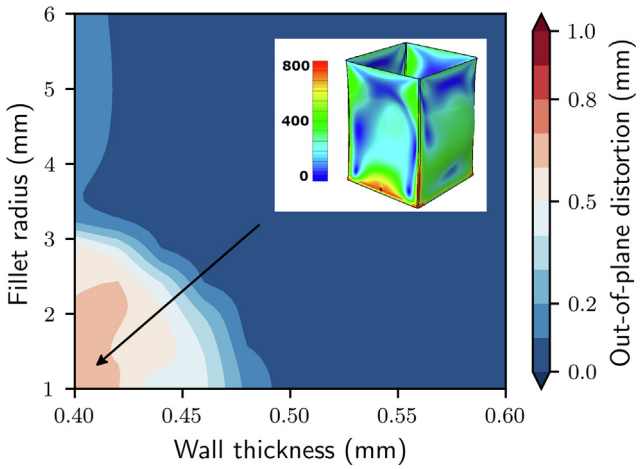

Fig. 8. Design map for thin wall of height 40 mm and width 30 mm. We note that the shorter height, at the same part width of Fig. 6, reduces distortion by preventing the part to fully develop out-of-plane distortion. Inset shows the actual part at wall thickness 0.4 mm and fillet radius 1 mm. Inset color represents von Mises stress in MPa.

From the figure, we would also like to note that the transition from not distorted to distorted components appears rather sharp, compared to the area of the map. Such transition suggests that a buckling mechanism may be responsible for the distortion, and motivates our further analysis reported later in the discussion.

Experimental measurements of distortion in form of 3D scanner data were compiled in Fig. 7. We see the qualitative and quantitative measured distortion matches the numerical predictions in terms of distortion of each tube as well as of the design map in Fig. 6, validating our analysis and modeling.

Exploration of the design space continued with the study of the role of wall height and wall width. Using the previous case (height

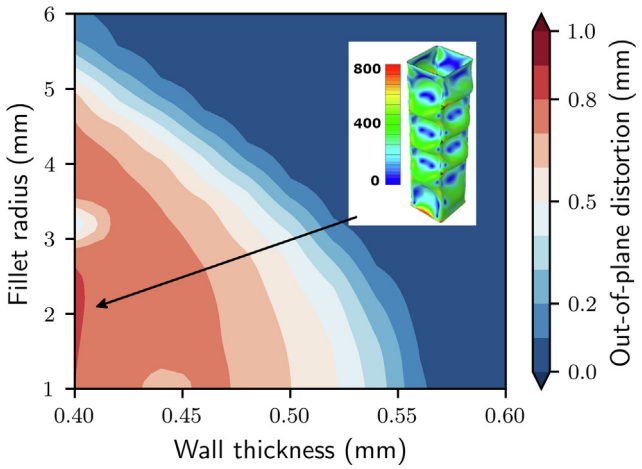

Fig. 9. Design map for part height 120 mm and part width 30 mm. In this case, distortion appears not to be quantitatively larger than for part height of 80 mm (Fig. 6), suggesting that out-of-plane deflection reaches a steady state during build. At the same time, the distorted region of the map is larger compared to the case of 80 mm, suggesting that tall parts are more susceptible to distortion, even if it is not quantitatively larger than for shorter parts. Inset shows the most distorted design, namely a fillet radius of 2 mm and wall thickness of 0.4 mm. Inset color represents von Mises stress in MPa.

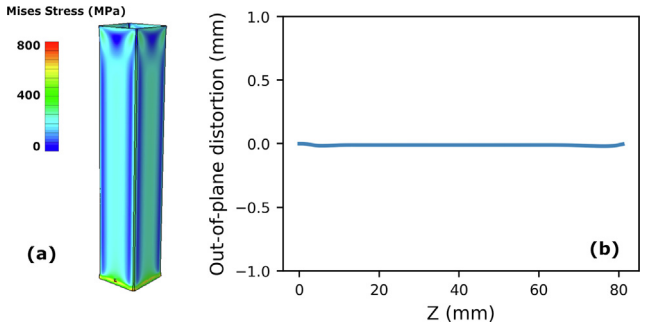

Fig. 10. (a) Residual stress and 3D rendering of wall thickness 400 μm, fillet radius 1 mm, part height 80 mm and width 15 mm. Color-coded is the Von Mises stress in MPa. (b) vertical line profile of out-of-plane distortion showing that, despite the challenging design parameters, no distortion is found.

area affected by distortion is larger compared to the 80 mm case. The rather abrupt onset of large out-of-plane displacement when part height increases is consistent with the buckling mechanism. Buckling occurs during the build and large distortions characterize post-buckled shapes, as compared to shorter parts having smaller buckling distortion. The buckling mode is investigated further after the presentation of design maps.

Next, the role of part width is discussed. For the case of 15 mm width (80 mm height), no significant distortion was found at any design combination, therefore, a distortion map is not reported. However, for completeness of analysis, the design with the most challenging parameters (i.e., wall thickness 400micron and fillet radius 1 mm) is shown in Fig. 10, confirming that no distortion was found for narrow parts. Such finding was interpreted by noting that part width appeared to be just not large enough to develop distortion, confirming that out-of-plane deflection is seen as an

80 mm, width 30 mm) as a reference, height was halved (40 mm) and increased 1.5 times (120 mm) at constant wall width (30 mm), followed by two additional cases where wall width was halved (15 mm) and increased 1.5 times (45 mm) at constant wall height (80 mm).

We begin by discussing the role of wall height, by reporting the design map for 40 mm and 120 mm part height in Fig. 8 and Fig. 9, respectively.

Fig. 8 shows that a lower height reduced both the area and the magnitude of distortion. We interpret this finding by commenting that a shorter height prevents the part from developing full out-of-plane distortion, in other words, the characteristic wavelength of out-of-plane distortion appears to be an intrinsic feature of the process, rather than being dictated by the part height.

On the other hand, the design map for 120 mm part height (Fig. 9) is revealing that tall parts do not exhibit quantitatively larger distortion compared to shorter parts (80 mm, Fig. 6). This finding suggests that distortion appears to reach a steady state with build height, after which it does not increase further. For a part width of 30 mm, the steady state appears to have reached between 80 and 120 mm. At the same time, Fig. 9 is also showing that the

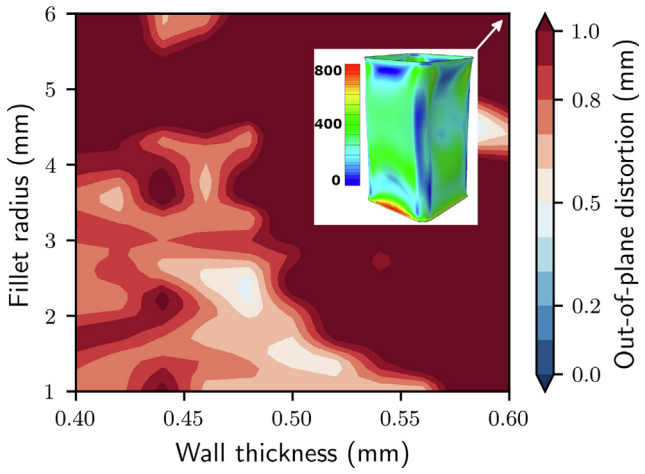

Fig. 11. Design map at part width 45 mm and height 80 mm. This map clearly shows an important role of part width in influencing distortion, more than part height. In fact, the whole map shows significant distortion, even at relatively thick wall and large fillet radiuses, at combinations where narrower parts do not distort. Inset shows the actual distorted part at wall thickness 0.6 mm and fillet radius 6 mm, showing that the distortion behaviour is also different from the case of same height but narrower part (Fig. 6). Inset color represents von Mises stress in MPa.

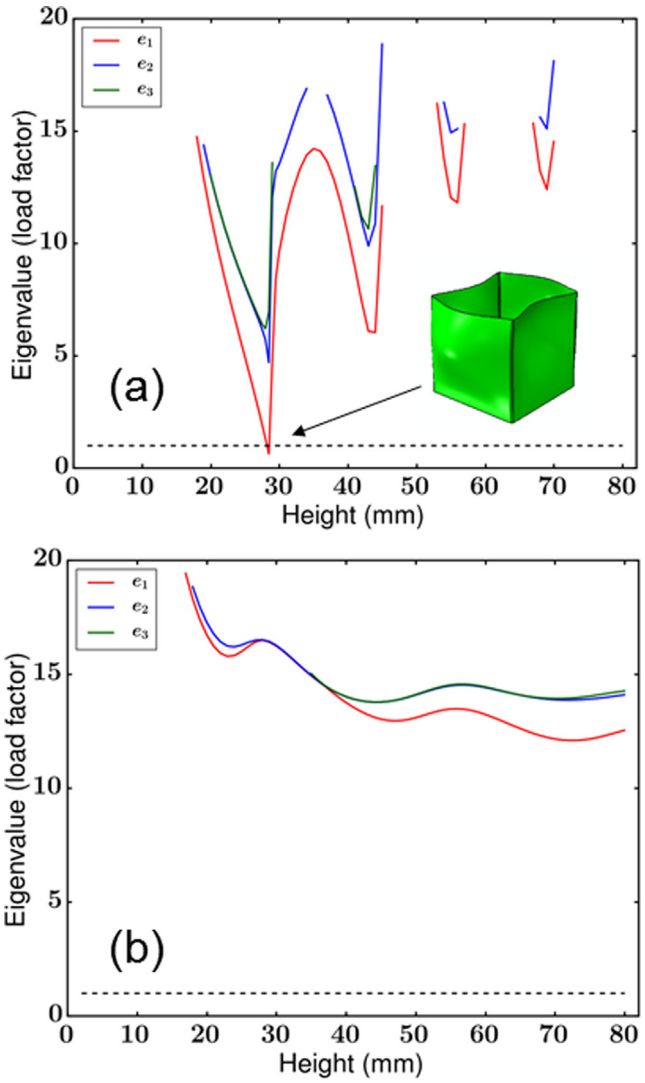

Fig. 12. First three positive lowest-energy eigenvalues for self-buckling of a thin wall structure with wall thickness 0.4 mm and fillet radius (a) 1 mm; (b) 6 mm. Panel (a) shows that an eigenvalue reaches one, and therefore this structure is expected to self-buckle at that height. The corresponding eigenshape is shown in inset, which agrees with the distorted shape predicted by direct layer-by-layer modeling. On the contrary, the shape in panel (b) has no eigenvalues reaching one, therefore, it is not expected to buckle. The heights without data points had no positive eigenvalues, and therefore they were not plotted. This analysis is in agreement with the distortion map of Fig. 6.

intrinsic feature of the process rather than developing equally at any combination of part width and height.

Finally, part width of 45 mm and height of 80 mm were studied, and its design map is reported in Fig. 11. Contrary to all the previous maps, a larger width shows significant emergence of distortion, even at combinations of thick walls and large fillet radiuses. Such finding shows us that part width is even more critical than part height in influencing distortion (Fig. 9), and therefore should be considered carefully when designing parts for powder-bed fusion additive manufacturing.

Linear elastic buckling analysis helps us understand the higher bending rigidity of cylindrical tubes compared to square tubes. For square cross-section tube of side width b and wall thickness h, the critical buckling stress for the lowest order mode is

$$\sigma_{c,sq} = \frac{k_w \pi^2 E}{12(1-\nu^2)} \left(\frac{h}{b}\right)^2 \tag{3}$$

and k_w is the buckling coefficient. For the square cross-section, $k_w = 4$ [32] and so

$$\sigma_{c,sq} = \frac{\pi^2 E}{3(1-\nu^2)} \left(\frac{h}{b}\right)^2 \tag{4}$$

For a circular cross section of radius a with the same cross-sectional area as the square tube ($\pi a^2 = b^2$), the critical buckling stress for the lowest order mode is [33]

$$\sigma_{c,cyl} = \frac{E}{\sqrt{3(1-\nu^2)}} \frac{h}{a} \tag{5}$$

Setting the geometrical parameters to $h = 0.5\ mm$ and $b = 30\ mm$ (refer to the following section for further details), the critical stress values are $\sigma_{c,sq} = 154\ MPa$, $\sigma_{c,cyl} = 2800\ MPa$, which confirms the higher load required to buckle a circular cross-section shape compared to a square one of equal cross-sectional area. This result can be rationalized by recalling that in-plane and out-of-plane displacements are decoupled in the deformation of thin plates, while they are coupled in the case of thin shells [33]. Intuitively, this property arises from the fact that buckling of shells requires the stretching of the diameter, which requires a significantly higher load compared to the simple out-of-plane bending for thin plates.

After performing this first step of validation, a buckling analysis was performed in the region of the design map most prone to distortion, namely, a wall thickness smaller than 0.6 mm and fillet radius smaller than 6 mm to understand if a critical height could exist below which distortion does not yet appear. We started with a wall thickness of 0.4 mm and a fillet radius of 1 mm. By performing 160 calculations (each one for a different part height), the plot in Fig. 12(a) was obtained. This figure shows that the lowest-energy eigenvalue is 1 at around 28 mm height: this was the predicted critical height for this particular wall thickness and fillet radius. To confirm this prediction, we extracted vertical displacement profiles before and after the 28 mm height, as shown in Fig. 13. The corresponding eigenshape, shown as inset in Fig. 12 (a), further confirms that the distorted shape predicted by the buckling analysis agrees with the one shown in Fig. 2.

A second configuration was chosen with a wall thickness of 0.4 mm and fillet radius of 6 mm, and the same buckling analysis was performed as described above. The result is shown in Fig. 12 (b). This panel shows that, in this case, the eigenvalues are systematically above one. Therefore, no buckling is predicted for such a design. Indeed, this shape does not distort significantly, as seen in Fig. 7.

Experimental investigation for the existence of a critical buckling height was performed for a thin wall tube with 0.4 mm wall thickness, 30 mm width, and 1 mm fillet radius. Two samples were built, with a height below and above the predicted critical height, respectively. Noting the numerical analysis results, the heights of 33 mm and 25 mm were chosen and the deformation measurement results are shown in Fig. 14. When compared to the predicted vertical distortion profiles (Fig. 13) for this particular wall thickness and fillet radius, the distortion in the printed sample confirms a significantly larger distortion for the taller sample, in both the inward as well as in the outward-distorted sides of the square tube, which doubles within an increase of height of less than 10 mm.

Supported by the agreement between the direct, layer-by-layer prediction of distortion and the predicted onset of buckling at a critical height, the numerical method described above was applied systematically to study buckling across the critical region shown in red color in Fig. 6. Here, the goal was to provide a design guideline for thin walls prone to distortion. By systematically setting a wall thickness and fillet radius and recording if an eigenvalue reached one and at which height, the critical height map shown in Fig. 15

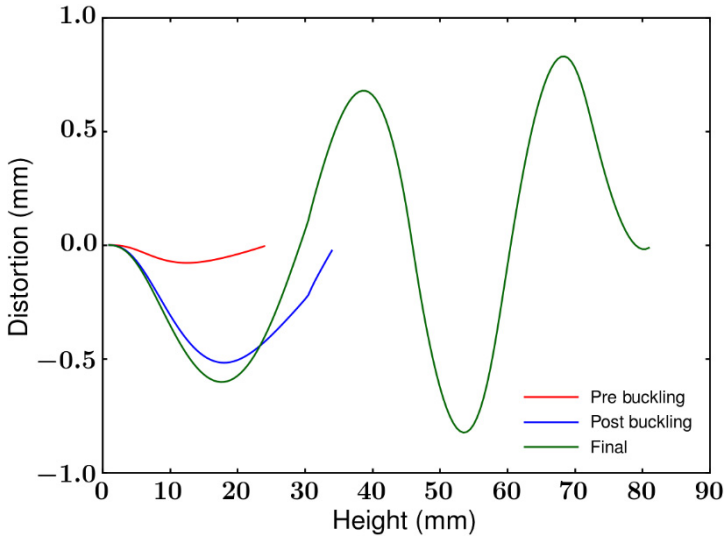

Fig. 13. Comparison of the vertical distortion profiles before and after the critical height for buckling is crossed (28 mm) for a thin wall of wall thickness 0.4 mm and fillet radius 1 mm, showing that the majority of distortion is already reached immediately after buckling, as compared to the final distortion.

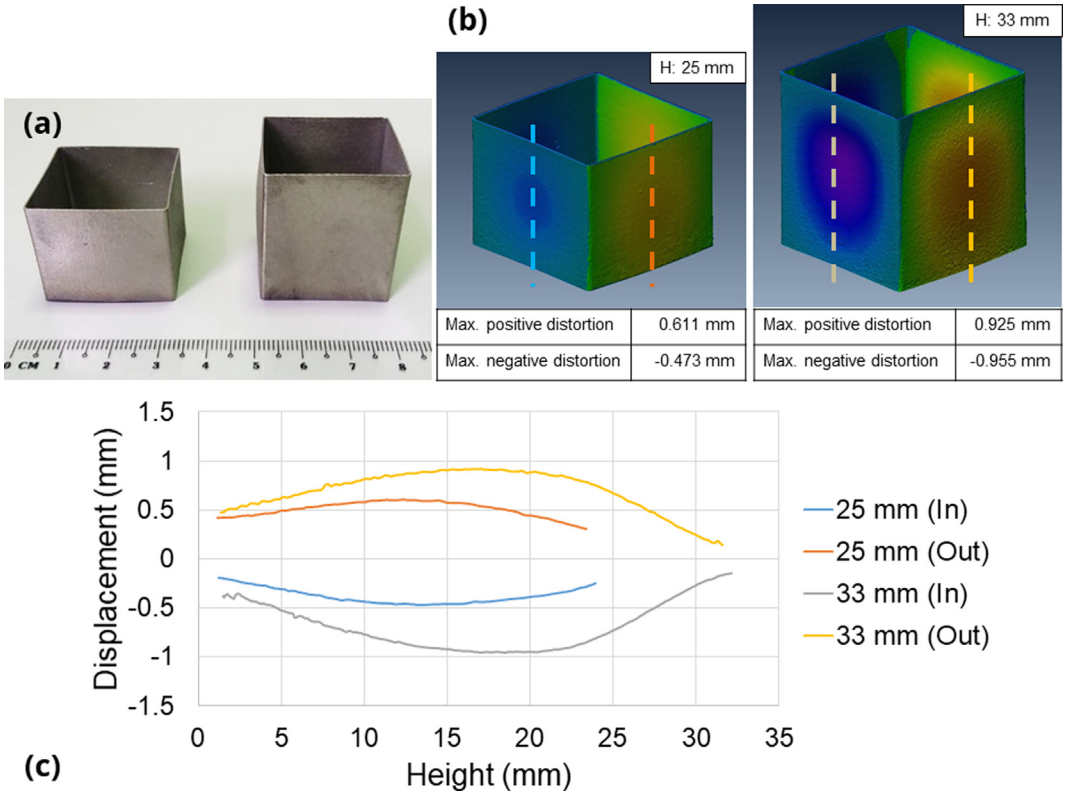

Fig. 14. (a) SLM printed thin wall tubes for critical buckling height validation. (b) Distortion as measured by laser scanner, where blue denotes distortion inwards the tube while red is distortion outwards the tube. (c) Distortion line profiles extracted along the dashed lines in panel (b), showing a noticeable increase in out-of-plane distortion after the critical height predicted numerically is crossed. (For interpretation of the references to color in this figure legend, the reader is referred to the web version of this article.)

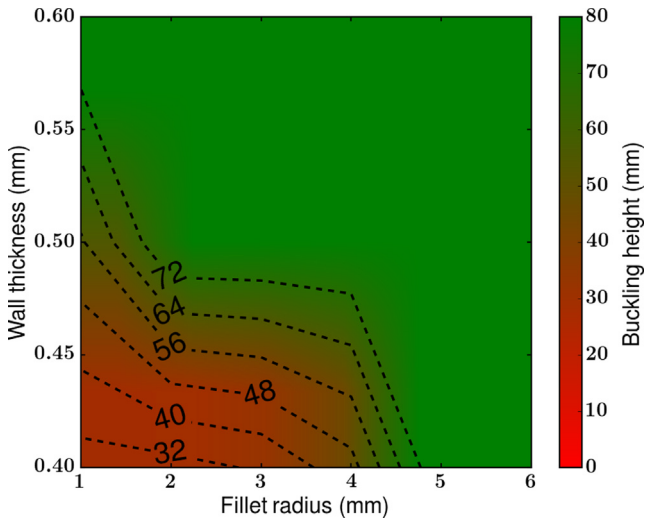

Fig. 15. Critical buckling height during additive manufacturing of thin wall tubes as a function of design shape, namely, wall thickness and fillet radius. This figure combines the result of 18 buckling calculations, each one performed as described in Sec. 2. In each calculation, wall width and height were kept constant at 30 mm and 80 mm, respectively.

was computed. In this map, color represents the critical height for buckling at each combination of wall thickness and fillet radius, at constant part width of 30 mm and height of 80 mm. This map provides a design tool for applications where very thin walls and small fillet radius are required, by identifying the height below which distortion is small.

4. Conclusions

In conclusion, a combined modeling and experimental study was carried out to explore design for additive manufacturing in powder-bed fusion processing of thin-wall structures. Using the inherent strain method, distortion was computed layer by layer and systematic calculations were performed whereby distortion was studied as a function of part design, namely, wall thickness, fillet radius, height, and width. Results were compiled into design maps, showing the critical role of fillet radius in reducing wall distortion. This is consistent with our understanding of mechanics that shows cylindrical tubes have higher buckling stress than square tubes. Exploration of part width shows narrow parts have consistently smaller distortion, even for small fillet radius and wall thickness, compared to wider parts. The actual build of the parts validated the predicted distortions for a given wall thickness and fillet radius and the qualitative trend in the design maps. Finally, numerical buckling analysis allowed us to identify a critical height for self-buckling and to rationalize large distortions as the result of post-buckling. The combined modeling and experimental results offer a comprehensive study of distortion and buckling in thin-wall structures and suggest design rules for the appropriate insertion of additively manufactured thin-wall structures into industrial production.

Declaration of Competing Interest

The authors declare that they have no known competing financial interests or personal relationships that could have appeared to influence the work reported in this paper.

Acknowledgements

We gratefully acknowledge the financial support of the A*STAR Aerospace Program through the project "Validated Models for Predicting Thin Wall Distortion and Evaluation of In-Process Monitoring for Defect Detection in Powder Bed Additive Manufacturing" (grant 1521500063) and the project "Industrial Digital Design and Additive Manufacturing Workflows" (grant A19E1a0097).

Data availability

The numerical and experimental raw data is available upon request from the corresponding author.

References

[1] Wohlers Associates, Wohlers Report, Wohlers Associates, Fort Collins, CO, USA¸2021.
[2] B. Blakey-Milner, P. Gradl, G. Snedden, M. Brooks, J. Pitot, E. Lopez, M. Leary, F. Berto, A. du Plessis, Metal additive manufacturing in aerospace: a review, Mater. Des. 209 (2021) 110008.
[3] O. Diegel, J. Schutte, A. Ferreira, Y. Lun Chan, Design for additive manufacturing process for a lightweight hydraulic manifold, Addit. Manuf. 36 (2020) 101446.
[4] S. Gill, H. Arora, S.V. Jidesh, On the development of Antenna feed array for space applications by additive manufacturing technique, Addit. Manuf. 17 (2017) 39–46.
[5] S. Daynes, J. Lifton, W.F. Lu, J. Wei, S. Feih, Fracture toughness characteristics of additively manufactured Ti–6Al–4V lattices, Eur. J. Mech.-A/Solids 86 (2021) 104170.
[6] B. Stucker, D.W. Rosen, I. Gibson, Additive Manufacturing Technologies: 3D Printing, Rapid Prototyping, and Direct Digital Manufacturing, Springer, Berlin, 2014.
[7] A. Prasad, L. Yuan, P. Lee, M. Patel, D. Qiu, M. Easton, D. StJohn, Towards understanding grain nucleation under Additive Manufacturing solidification conditions, Acta Mater. 195 (2020) 392–403.
[8] L. Cheng, A. To, Part-scale build orientation optimization for minimizing residual stress and support volume for metal additive manufacturing: Theory and experimental validation, Comput. Aided Des. 113 (2019) 1–23.
[9] M. Brennan, J. Keist, T. Palmer, Defects in Metal Additive Manufacturing Processes, J. Mater. Eng. Perform. 30 (2021) 4808–4818.
[10] N.E. Hodge, R.M. Ferencz, J.M. Solberg, Implementation of a thermomechanical model for the simulation of selective laser melting, Comput. Mech. 54 (2014) 33–51.
[11] N.E. Hodge, R. Ferencz, R. Vignes, Experimental comparison of residual stresses for a thermomechanical model for the simulation of selective laser melting, Addit. Manuf. 12 (2016) 159–168.
[12] P. Prabhakar, W. Sames, R. Dehoff, S. Babu, Computational modeling of residual stress formation during the electron beam melting process for Inconel 718P, Addit. Manuf. 7 (2015) 83–91.
[13] G. Vastola, G. Zhang, Q.X. Pei, Y.W. Zhang, Controlling of residual stress in additive manufacturing of Ti6Al4V by finite element modeling, Addit. Manuf. 12 (2016) 231–239.
[14] Z. Wang, W. Yan, W.K. Liu, M. Liu, Powder-scale multi-physics modeling of multi-layer multi-track selective laser melting with sharp interface capturing method, Comput. Mech. 63 (4) (2019) 649–661.
[15] Y.P. Yang, M. Jamshidinia, P. Boulware, S.M. Kelly, Prediction of microstructure, residual stress, and deformation in laser powder bed fusion process, Comput. Mech. 61 (5) (2018) 599–615.
[16] J. Heigel, P. Michaleris, E. Reutzel, Thermo-mechanical model development and validation of directed energy deposition additive manufacturing of Ti–6Al–4V, Addit. Manuf. 5 (2015) 9–19.
[17] X. Guan, Y.F. Zhao, Modeling of the laser powder–based directed energy deposition process for additive manufacturing: a review, Int. J. Adv. Manuf. Technol. 107 (2020) 1959–1982.
[18] H. Huang, Y. Wang, J. Chen, Z. Feng, A Comparative Study of Layer Heating and Continuous Heating Methods on Prediction Accuracy of Residual Stresses in Selective Laser Melted Tube Samples, Integrating Materials and Manufacturing Innovation 10 (2) (2021) 218–230.
[19] M.K. Thompson, G. Moroni, T. Vaneker, G. Fadel, R.I. Campbell, I. Gibson, A. Bernard, J. Schulz, G.P.B. Ahujai, F. Martina, Design for Additive Manufacturing: Trends, opportunities, considerations, and constraints, CIRP Annals - Manufacturing Technology 65 (2016) 737–760.
[20] T. Yang, D. Xie, W. Yue, S. Wang, P. Rong, L. Shen, J. Zhao, C. Wang, Distortion of Thin-Walled Structure Fabricated by Selective Laser Melting Based on Assumption of Constraining Force-Induced Distortion, Metals 9 (2019) 1281.
[21] F. Calignano, G. Cattano, D. Manfredi, Manufacturing of thin wall structures in AlSi10Mg alloy by laser powder bed fusion through process parameters, J. Mater. Process. Technol. 255 (2018) 773–783.
[22] A. Ahmed, A. Majeed, Z. Atta, J. Guozhu, Dimensional Quality and Distortion Analysis of Thin-Walled Alloy Parts of AlSi10Mg Manufactured by Selective Laser Melting, J. Manuf. Mater. Process. 3 (2) (2019) 51.
[23] S.M. Thompson, Z.S. Aspin, N. Shamsaei, A. Elwany, L. Bian, Additive manufacturing of heat exchangers: a case study on a multi-layered Ti–6Al–4V oscillating heat pipe, Addit. Manuf. 8 (2015) 163–174.
[24] M. Kilian, C. Hartwanger, M. Schneider, M. Hatzenbichler, Waveguide components for space applications manufactured by additive manufacturing technology, IET Micro. Ant. & Prop. 11 (14) (2017) 1949–1954.
[25] M. Hill, D. Nelson, The inherent strain method for residual stress determination and its application to a long welded joint, Stanford University, 1999.
[26] H. Murakawa, D. Deng, N. Ma, J. Wang, Applications of inherent strain and interface element to simulation of welding deformation in thin plate structures, Comput. Mater. Sci. 51 (2012) 43–52.
[27] A. Khurram, K. Shehzad, FE Simulation of Welding Distortion and Residual Stresses in Butt Joint Using Inherent Strain, Int. J. Appl. Phys. Math. 2 (6) (2012) 405–408.
[28] C.D. Jang, Y.T. Kim, Y.C. Jo, H.S. Ryu, in: 10th International Symposium on Practical Design of Ships and Other Floating Structures, Houston, TX, USA, 2007.
[29] T.-J. Kim, B.-S. Jang, S.-W. Kang, Welding deformation analysis based on improved equivalent strain method considering the effect of temperature gradients, Int. J. Naval Architecture Ocean Engin. 7 (1) (2015) 157–173.
[30] E. Denlinger, P. Michaleris, Effect of stress relaxation on distortion in additive manufacturing process modeling, Addit. Manuf. 12 (2016) 51–59.
[31] EOS, "EOS Inconel® 718 Material Datasheet," EOS GmbH Electro Optical Systems, Krannling, 2020.
[32] T. Wierzbicki, "Lecture notes on Plates and Shells," [Online]. Available: https://ocw.mit.edu/courses/mechanical-engineering/2-081j-plates-and-shells-spring-2007/readings/lecturenote.pdf.
[33] S. Timoshenko, S. Woinowsky-Krieger, Theory of Plates and Shells, McGraw-Hill, 1959.